Published in final edited form as:
J Microelectromech Syst. 2011 October 1; 20(5): 1119–1130. doi:10.1109/JMEMS.2011.2162487.

A Fully-Passive Wireless Microsystem for Recording of Neuropotentials using RF Backscattering Methods

Helen N. Schwerdt,
School of Electrical, Computer, and Energy Engineering at Arizona State University, Tempe, AZ 85287 USA

Wencheng Xu,
School of Electrical, Computer, and Energy Engineering at Arizona State University, Tempe, AZ 85287 USA

Sameer Shekhar,
ASU at the time of performing this research. He is currently with Intel Corporation, Hillsboro, OR USA.

Abbas Abbaspour-Tamijani[Senior Member, IEEE],
ASU at the time of performing this research. He is currently with Freeform Wave Technologies, LLC, Los Angeles, CA 90049 USA.

Bruce C. Towe,
School of Biological and Health Systems Engineering at Arizona State University, Tempe, AZ 85287 USA.

Félix A. Miranda[Senior Member, IEEE], and
NASA Glenn Research Center, Cleveland, OH 44135 USA.

Junseok Chae[Member, IEEE]
School of Electrical, Computer, and Energy Engineering at Arizona State University, Tempe, AZ 85287 USA

Abstract

The ability to safely monitor neuropotentials is essential in establishing methods to study the brain. Current research focuses on the wireless telemetry aspect of implantable sensors in order to make these devices ubiquitous and safe. Chronic implants necessitate superior reliability and durability of the integrated electronics. The power consumption of implanted electronics must also be limited to within several *milliwatts* to *microwatts* to minimize heat trauma in the human body. In order to address these severe requirements, we developed an entirely passive and wireless microsystem for recording neuropotentials. An external interrogator supplies a fundamental microwave carrier to the microsystem. The microsystem comprises varactors that perform nonlinear mixing of neuropotential and fundamental carrier signals. The varactors generate third-order mixing products that are wirelessly backscattered to the external interrogator where the original neuropotential signals are recovered. Performance of the neuro-recording microsystem was demonstrated by wireless recording of emulated and *in vivo* neuropotentials. The obtained results were wireless recovery of neuropotentials as low as approximately 500 microvolts peak-to-peak (μV_{pp}) with a bandwidth of 10 Hz to 3 kHz (for emulated signals) and with 128 epoch signal averaging of repetitive signals (for *in vivo* signals).

Correspondence to: Helen N. Schwerdt.
(corresponding author hschwerd@asu.edu)..

Keywords

neural telemetry; bio-MEMS; neural recording; backscattering; radio frequency identification (RFID)

I. Introduction

The aim of developing wireless neuro-interfaces is to resolve complex challenges underlying basic underst anding and treatment of the central nervous system (CNS). Neuro-interfacing enables scientists to probe into the brain and form a direct causal link between a person's behavior and the highly complex network of billions of neurons making up the CNS. Neuro-interfacing embodies both the recording and the stimulation of neurons for closed-loop interaction with the brain. Neuro-recording implies “recording” of electrical activity produced by neurons. It involves, more specifically, acquiring extracellular action potentials, i.e., neuropotentials, propagating down branch-like extensions of neurons, the axons. When the neuropotentials are acquired from the brain's outermost layer, the cerebral cortex, the potentials are denoted as electrocorticographic (ECoG) signals. The ECoG signals typically are on the order of several *microvolts* and within a few *Hz* to thousands of *Hz* and are correlated with the most active region of the brain [1]. Early stage clinical applications of cortical neuro-recording systems have revealed important discoveries in the field of neuroscience and neurology [2], [3], and also manifested into important prosthetic and rehabilitative remedies for patients suffering from a range of disabilities rooted in the CNS [4]. Nevertheless, before these systems can be viably adopted into the clinical setting, they must conform to the stringent requirements demanded for safe and chronic implantation. To this end, the proposed neuro-recorder attempts to address these requirements through design of a MEMS (Micro-Electro-Mechanical-Systems)–based fully-passive circuit capable of wireless telemetry of neuropotentials.

Wireless neuro-recording microsystems typically comprise microelectrodes to probe the neurons, complex circuitry to amplify the substantially low neuropotentials and to process and prepare these signals for wireless telemetry, and a wireless link (antenna or inductive coil) to transmit the neuropotential signals [5]. The integrity of neuropotential recording and wireless transmission commonly necessitates sophisticated mixed-signal circuitry [6], [7]. However, the level of circuit complexity is multiplied for multichannel operation, and neural applications often require dozens to hundreds of channels. Furthermore, the number of channels is directly correlated to the amount of power consumption, which in turn determines the degree of heat dissipation. The allowable rise in temperature in the cortex is 1 to 2 °C, which for a typical CMOS chip with a volume of 70 mm^3 placed on the cerebral cortex, translates to a maximum allowable heat dissipation of 10 mW [5]. In order to circumvent heat emanation into the cortex, the microelectronic circuit component is usually embedded just beneath the scalp and wired into the skull to physically connect with the electrodes penetrating the cortex [8], [9]. In order to remove these interconnects and lessen signal loss associated with this external wiring, some groups have monolithically integrated the circuits onto the electrodes, fabricated die-level post-CMOS electrode s o n-chip, or manually combined the circuits and the electrodes [10]-[12]. Regardless of the approach, most of these microsystems inevitably lead to either heat trauma or potential risk of device failure or physical trauma attributed to tethering forces and associated movement from the surgical wiring through the skull [5], [11].

The mode in which wireless transmission is realized in implantable microsystems may be distinguished by three categories; active, passive, and fully-passive systems. Active systems contain an internal energy source, a small rechargeable battery or energy harvester, which

supplies all of the power needed to operate enclosed circuitry [8], [13], [14]. However, in terms of implantable systems, several drawbacks are immediately apparent; the internal energy source increases the overall size of the implant, batteries will need to be recharged or replaced, and energy harvesting sources usually require additional power regulation circuitry that again enlarges the implant size.

More recently, passive schemes have been adopted in an attempt to diminish heat dissipation, shrink the footprint, and extend the lifetime of the implant [15]-[17]. Passive systems extract power exclusively from external sources through electromagnetic (EM) radiation from an antenna or magnetic flux from an inductive coil. As a result, no internal battery or harvester is needed. Passive systems are increasingly being exploited in RFID (Radio Frequency Identification) technology, where low-cost and long-term properties are targeted features of the sensing and identification RFID tags. Because of the reliability and multi-functionality provided by the integrated digital electronics, active and passive techniques are employed in the majority of existing wireless neuro-recording microsystems and have been successfully implemented in numerous animal tests [14], [15], [18].

In this work, “fully-passive” terminology is used to describe a particular type of passive system free of any formal energy source. That is, a fully-passive system does not need to regulate or rectify externally generated power in order to activate onboard circuitry. As a result, sophisticated and complex circuitry is completely excluded. Since the fully-passive circuits dissipate little of the induced power, they have the potential to reduce risks associated with power dissipation in implants. In the present device design, neuropotentials modulate an externally generated carrier by means of nonlinear elements, such as varactors. The modulated carrier, conveying the internal neuropotential signal, is backscattered to an external detector that can demodulate and recover the original neuropotential signal. This backscattering effect has been utilized in both the active and passive schemes, and is pervasive in RFID technology [19], [20]. However, in the fully-passive case, the backscattering effect becomes of predominant interest since the fully-passive device alone does not generate any radio frequency (RF) signals. Its most notable success was demonstrated in the widely-commercialized, fully-passive arterial pressure sensors, which have been implanted in over a hundred patients [21]. Fully-passive devices have also found application in sensing *in vivo* electrical signals generated by the heart, electrocardiography (ECG), or the brain, ECoG or electroencephalography (EEG) [22]-[24].

The idea of using voltage sensitive elements for wireless biological telemetry dates back to 1965 [25]. The technique was reintroduced in 2007 when the idea was materialized through the use of off-shelf varactors and an inductor for wireless fully-passive transmission [22]. More recently, the technique was applied to wirelessly record ECG externally from humans [24]. These devices rely on inductive coupling for wireless telemetry. Inductive coupling is an attractive technique because of its relatively high efficiency as compared to the EM propagation method of wireless communication. Inductive coupling seems a natural choice when the interrogator operates at low frequencies, i.e., below 1 GHz, where the equivalent EM operating antenna may become too large for an implantable device. The efficiency of wireless inductive coupling is primarily determined by the geometry of both coils, the magnetic properties (permeability) of the transmission media, and the relative placement of the coils. The amount of induced magnetic flux is not affected by the transmission media as the permeability of biological and free-space media is nearly unity and the flux is not a function of the dielectric properties (permittivity) of the media. However, it is very sensitive to the relative placement of the primary and secondary coils [26]. At higher frequencies, i.e., above 2 GHz, inductive coils can be replaced by antennas where RF energy propagates as EM waves. Although the signal experiences more attenuation through tissue as frequency increases, the internal efficiency of the antenna also increases [23]. Due to these opposing

trends, for a given area, migrating to a higher frequency can potentially improve the overall efficiency of EM transmission. The optimal frequency will ultimately depend on the specific design of the antenna as well as the thickness and electrical properties of the intermediate tissues between the interrogator and implant. This EM propagation method, previously rendered on a printed circuit board (PCB), produced encouraging results for an interrogation frequency of 2.48 GHz [23].

The device proposed here uses microfabrication techniques to minimize its footprint, maximize fabrication throughput, and minimize the number of off-chip components. We evaluate its characteristics and potential feasibility as an implantable sensor through results acquired from recording neuropotentials from frogs. We also evaluate its potential for ECoG and similar neuro-recording applications.

II. Materials and Methods

The wireless neuro-recording system consists of two components: 1) the neuro-recording and backscattering microsystem, and 2) the external dual-band interrogator. Unlike inductive coupling, backscattering in the form of radiating EM waves strongly depends on the electrical properties of the media through which the waves propagate, especially at microwave frequencies. These properties alter the impedance of the internal antenna and govern a major portion of the path loss experienced by the RF signal. Furthermore, the path loss increases as wavelength decreases (frequency increases) and as the depth of tissue penetration increases. In this work, the intent of utilizing higher microwave frequencies is to minimize the size of the antenna integrated onto the microsystem. As the antenna impedance is a function of the medium in which it is operating, the properties of the biological tissue must be taken into account in the design of the backscattering system. The neuro-recording microsystem was fabricated on a high resistivity silicon substrate using standard microfabrication techniques.

A. Microwave Backscattering in Biological Media

Transmission media include the several organic layers enclosing the brain as well as free-space (air). The relative permittivity (ε_r) of the cutaneous and subcutaneous tissue, skull, meninges, cerebrospinal fluid (CSF), and the cortex, can vary from 30 to 65 and depends on the frequency of the pervading microwave signals [27], [28]. Variations in ε_r directly alter the wavelength and phase velocity of the wireless signals. The conductivity (σ) varies from 0.5 to 2 S/m accounting for real power losses in the radiating waveform. In frequency ranges above the *MHz* regime, dipolar orientation of water molecules in tissues tends to dominate the dielectric permittivity of the material. The frequency dependence of the complex permittivity can be modeled using the Cole-Cole equation [29],

$$\widehat{\varepsilon}(\omega)=\varepsilon' - j\varepsilon''=\varepsilon_\infty+\frac{\varepsilon_s-\varepsilon_\infty}{1+(j\omega\tau)^{1-\alpha}}+\frac{\sigma}{j\omega\varepsilon_0} \quad (1)$$

where ε' is the real part of the permittivity, ε'' is the imaginary part of the permittivity, ε_∞ is the permittivity at $\omega\tau \gg 1$, ε_s is the permittivity at $\omega\tau \ll 1$, ε_0 is the permittivity of free-space ($\varepsilon_0 \approx 8.854\times10^{-12}$ *F/m*), α is the distribution parameter, and τ is the relaxation time. From (1), radiation losses through the materials surrounding the cortex can be computed for a given frequency. As the frequency increases, signal loss, due to material or volume conductivity, increases, and this can be estimated by the EM skin depth, defined as the depth at which current density decreases by $1/e \approx 0.37$ compared to its value at the surface and given by [30],

$$\delta = \frac{1}{\mathrm{Im}\left[\sqrt{\omega\mu(\omega\hat{\varepsilon} - j\sigma)}\right]} = \frac{1}{\mathrm{Im}\left[\sqrt{\omega^2\mu\varepsilon' - j\omega\mu(\omega\varepsilon'' + \sigma)}\right]} \quad (2)$$

As the denominator increases with frequency, skin depth becomes smaller. This points to a clear tradeoff in the link budget; higher frequencies allow implementing more efficient antennas on a typically small implant, whereas lower frequencies allow minimization of signal loss in the body. The roundtrip path loss associated with backscattering microwaves through the human head has been modeled, indicating the existence of an optimal frequency of operation near 3 GHz [23].

B. Design of Neuro-Recording and Backscattering Microsystem

A passive harmonic mixer frames the basic operation of the neuro-recording and backscattering microsystem (Fig. 1). This mixer inputs the neuropotential signals and incident microwaves at the intermediate frequency (IF) port and local oscillator (LO) port, respectively. The mixer combines these two signals (f_m at IF and f_0 at LO) and upconverts them to $2f_0 \pm f_m$, at the RF port. The third-order intermodulation (IM3) products, $2f_0 \pm f_m$, are wirelessly backscattered to the external interrogator in the form of amplitude modulated (AM) transmission where they are downconverted and demodulated (Fig. 1a). A more straightforward mixing scheme may be applied to generate the first harmonics, $f_0 \pm f_m$ [24]. However, neuropotentials occupy a low frequency spectrum between 1 Hz to several *kHz* (IF) and are typically on the order of several tens of microvolts in amplitude (V_m). The incident microwaves (LO), on the other hand, are relatively higher in magnitude in comparison to the IF/RF signals. Unlike magnetic fluxes, as associated with inductive coupling, EM waves physically reflect from surrounding surfaces including the interfaces between different biological media [31]. These structural reflections manifest into electrical noise causing interference and desensitization especially near the LO band (f_0). Therefore, it is preferable to separate the neuropotential signals from these strong reflections by transmitting the information using higher-order mixing products. Details on the microsystem's mixing and backscattering of third-order harmonics are laid out in the following sub-sections.

Neuro-Recording Circuit—The neuro-recording circuit comprises of two M/A-COM MA46H120 varactors (C_V), a bypass capacitor (C_B), and an integrated antenna that for circuit design purposes can be represented by an impedance component (Z_A), as depicted in Fig. 1b. The varactor pair acts as a nonlinear mixer that is responsible for generating harmonic mixing products. The on-chip antenna acts as both the LO and RF interfaces for the mixer, while the neuro-probe (electrode-tissue interface and source for neuropotential signals) acts as the IF port. The bypass capacitor decouples the RF and LO signals from the IF port, effectively short circuiting the neuro-probe at high frequencies. The antenna itself has a near zero impedance at DC, which effectively short circuits the radiation ports at the low frequencies. The antenna is implemented as a capacitively-loaded slot antenna to allow proper optimization of its impedance at LO and RF frequencies.

A layout of the entire microsystem less the loading capacitors, varactors, and bypass capacitor was produced and simulated in High Frequency Structure Simulator (HFSS, Ansoft Corporation) (Fig. 1c). The result is incorporated into a schematic circuit model including the varactors, bypass capacitor, and parasitic elements. This circuit model can be analyzed in Advanced Design System (ADS, Agilent Technologies) environment using harmonic balance simulations to verify generation of targeted harmonic mixing products ($2f_0 \pm f_m$). Parameters of the dielectric films, substrate, antenna, and biological media were

included in the HFSS model, which solves Maxwell's equations in the structure using finite element method (FEM). This simulation produced s-parameters at the IF port (feed-through electrodes), pair of varactor ports (trench pads for mounting varactors and connection to antenna), pair of loading Metal-Insulator-Metal (MIM) capacitor ports (across antenna slot), and the LO and RF port (the latter two designated as a single wave port above the surface of the modeled scalp), which were then imported back into the ADS schematic environment to optimize the value of the loading capacitors for maximal backscattering at the RF frequency. Fig. 2a displays a simplified ADS schematic (not including ports for loading capacitors) utilizing a 4-port s-parameter element to import the high frequency characteristics from the varactor ports, IF port, and mutual LO and RF port. The predicted spectral response from ADS simulations is shown in Fig. 2b. The top plot shows the simulated harmonic balance mixing response for an optimized microsystem with an input (IF) sinusoidal neuropotential of V_m of 100 μVpp sinusoidal at f_m of 1 kHz, and LO incident power of P_0 of 1 mW (0 dBm) at f_0 of 2.4 GHz. The top plot also includes all of the possible harmonic mixing products greater than -200 dBm, including second-order intermodulation products of $f_0 \pm f_m$. The bottom plot shows a close-up of the targeted third-order mixing products $2f_0 \pm f_m$, depicting a predicted signal-to-noise ratio (SNR) of 30 dB (assuming a noise floor of -135 dBm). The simulations do not take into account various wireless environmental disturbances, such as noise or structural reflections.

A varactor is in essence a voltage variable capacitor; varying its capacitance as a function of the voltage applied across it. The nonlinear relation between applied voltage and varactor capacitance generates correlated harmonics. The capacitance of a varactor is expressed as,

$$C_v(V_r) = \frac{C_j}{\left(1+\frac{V_r}{V_j}\right)^{\gamma}} + C_p, \tag{3}$$

where V_r is the reverse-bias applied voltage, V_j is the junction voltage intrinsic to the device, γ is the gamma coefficient associated with doping parameters, C_p is the parasitic capacitance of the package, and C_j is the junction zero-bias capacitance [32]. The gamma coefficient, γ, controls the nonlinear characteristics. The nonlinear capacitance produces a host of nonlinear mixing products, including the third-order terms at $2f_0 \pm f_m$, whose amplitude is proportional to $V_0^2 V_m$ and constitute the desired backscattering signals. The input of the present system may be described as a superposition of the neuropotential ($V_m cos(\omega_m t)$) and incident microwave signals ($V_0 cos(\omega_0 t)$); $V = V_0 cos(\omega_0 t) + V_m cos(\omega_m t)$. Equation (3) may be expanded into a Taylor Series and substituted into the current-voltage relation, $I = d/dt[C(V)V]$, to approximate the harmonic current output of the varactor;

$$\begin{aligned} I &= \frac{d}{dt}\left(\sum_{n=1}^{\infty} c_n V^n\right) V, \\ I &= \frac{d}{dt}\left(c_1 + c_2 V + c_3 V^2 + \ldots\right) V, \\ I &= (c_{1a}+c_{3a}) \sin(\omega_0 t) + (c_{1a}+c_{3a}) \sin(\omega_m t) + c_{2a} \sin(2\omega_0 t) + c_{2b} \sin(2\omega_m t) + c_{2c} \sin(\omega_0 t \pm \omega_m t) + c_{3b} \sin(2\omega_0 t \pm \omega_m t) \end{aligned} \tag{4}$$

where the coefficients, c_n, determine the magnitude of the respective nth-order harmonics, and the subscripts, a and b, denote the combination of the capacitance coefficient with the

given amplitude, V_0 and V_m, of the inputted harmonics. A high c_3 is desirable to augment the magnitude of the third-order backscattering signals $c_{3b}sin(2\omega_0 t \pm \omega_m t)$, and is determined by γ, V_m, and V_0. The conversion gain of the system ($G_{2\omega}$), defined as the ratio of the power in these third-order backscattering terms to that of the information signal (V_m), is a function of the LO power, varactor's γ, and impedance values seen by the varactor at different frequencies. $G_{2\omega}$ is generally used to describe the efficiency of a mixer system. The choice of the varactor, design of the antenna, bypass capacitor and loading capacitors, electrode-tissue interface, and the biological media all impact that value of the conversion gain.

Although the varactor nonlinearity generally can produce all of the possible harmonics and mixing products of ω_0 and ω_m, it can be shown that the use of two varactors in back-to-back configuration helps reduce even-order harmonics and mixing terms, particularly the $2\omega_0$ term that interferes with the targeted third-order mixing products. This interference is mostly due to the phase noise associated with the second-order harmonic causing the magnitude of this signal to "jitter" around this frequency band and, in this case, into the nearby targeted sidebands of $\pm f_m$. Ideally, the use of matched back-to-back varactors leads to an even expression for $C(V)$, guaranteeing that the varactor current is an odd function of the voltage. In such circumstances the varactor current will only contain odd-order harmonics and mixing products, and will exclude terms such as $2\omega_0$. In practice, any mismatch between the varactors or asymmetry in their placement in the circuit can impair this condition, giving rise to a finite output at $2\omega_0$ and other even mixing terms. It should be noted that (4) is a simplified expression of the varactor output, as the exact harmonic output cannot be expressed in closed-form and is elaborated in previously published work [33]. The varactor's ability to produce third-order harmonics will influence the design of the integrated antenna and its overall backscattering response, which will be described in the next sub-section.

Integrated Antenna—A sub-resonant slot antenna is integrated onto the neuro-recording microsystem to operate at an incident frequency (f_0) around 2.25 to 2.45 GHz and a backscatter frequency ($2f_0 \pm f_m$) around 4.5 to 4.9 GHz. The antenna's slot is 10 mm in length and 1 mm in width and is loaded with a pair of MIM capacitors, used to optimize the impedance of the antenna for the best conversion gain. These MIM capacitors effectively lengthen the dimensions of the slot at the LO frequency and shorten it at the RF frequency. In free-space media the wavelength of the incident microwave signals at 2.45 GHz is approximately 12.2 cm. For a resonant antenna, the slot size should equal half the wavelength ($\lambda/2$), 6.1 cm [34]. When EM waves pervade through biological transmission media, the permittivity (ε) increases, and as a result, wavelength decreases by a factor of $\varepsilon^{-0.5}$. For the slot radiating inside the biological tissue, including layers of CSF, bone, fat, and skin, the effective wavelength is a fraction of the free-space value, but still large enough to make the 10 mm long slot sub-resonant.

For an electrically small antenna (ESA), where the maximum dimension is less than $\lambda/2\pi$ (about 19.4 mm for 2.45 GHz in free space), bandwidth and gain are severely compromised [35], [36]. The directivity of a short slot antenna with infinite ground is 1.76 dBi. The overall gain is usually 1 to 3 dB lower than this value, due to losses in the metal and silicon substrate.

In order to effectively transmit neuropotential signals, the external interrogator needs to emit a sufficient amount of incident power and the neuro-recorder should efficiently modulate and reflect this power. An antenna's ability to reflect power may be evaluated by its radar cross section [34],

$$\sigma=4\pi r^2\frac{S_b}{S_i}=G_{2\omega}\frac{\lambda^2}{4\pi}D_rD_te_re_t, \tag{5}$$

where the subscripts *r* and *t* correspond to reader (external interrogator) and transponder (neuro-recorder), respectively. *r* is the distance between the external interrogator and the neuro-recorder, S_i and S_b represent the incident and backscattered power flux densities, respectively (magnitude of the Poynting vector or cross product of electromagnetic waves; $S=|\vec{E}\times\vec{H}|$), $G_{2\omega}$ represents the conversion gain of wireless transmission from f_0 to $2f_0\pm f_m$ and its value is less than unity for passive systems, and λ is the wavelength of the EM wave transmitted to the neuro-recorder in the media that surrounds it. D_r and e_r are the directivity and efficiency of the antenna at f_0, and D_t and e_t are those at $2f_0\pm f_m$. The power of the useful backscattered signal from the microsystem (P_{bs}) can be calculated as the product of incident power density (S_i) and the radar cross section (σ). Certainly, both incident and backscattered signal undergo propagation losses, which must be taken into account in overall link calculation, and relating the incident and backscattered power densities to the transmitted and received powers requires including the transmit and receive gain of the reader antenna. But, none of these properties affects the design of the microsystem. In order to increase P_{bs}, σ needs to be maximized. From (5), this may be accomplished by increasing the directivities (D_t and D_r), efficiencies (e_t and e_r), and/or conversion gain ($G_{2\omega}$) associated with the strength of the nonlinear mixing of the varactors and impedance properties of the antenna and substrate. As was mentioned earlier, the directivity of short slot antennas is largely fixed at 1.76 dBi, and there is little room to improve the efficiency besides changing the frequency. Nevertheless, $G_{2\omega}$ can be increased by stronger nonlinear properties of the varactors and optimizing the impedance of the antenna at f_0 and $2f_0\pm f_m$. These parameters are optimized through the design of the integrated antenna in HFSS and optimization of the overall circuit is performed in ADS. The purpose of the MIM capacitors introduced towards the ends of the slot (Fig. 1c) is to provide the degrees of freedom needed to allow this optimization. Furthermore, enhancing the parameters of the external antenna will relieve some of the limitations associated with the integrated microsystem antenna, as will be discussed in the next section.

C. External Dual-Band Interrogator

The external dual-band interrogator utilizes a linearly tapered slot antenna (LTSA) to support the wireless system's wideband characteristics [37], [38]. The LTSA was designed in HFSS to optimize the antenna's efficiency to sufficiently radiate EM energy at LO (f_0) and receive the backscattering signals at RF ($2f_0\pm f_m$). As shown in Fig. 3a, the return loss (S(1,1)) is greater than 7 dB for 2.3 to 2.7 GHz and 4.6 to 5.5 GHz denoting less than 1 dB mismatch loss in either transmit or receive links when the interrogator operates at the fundamental incident frequency of 2.3 to 2.7 GHz. The mismatch effect is minimal for the interrogator operating at 2.45 to 2.6 GHz. In order to isolate transmit and receive channels, the LTSA is connected to a diplexer stage, comprising a low pass filter (LPF) operating in the incident frequency band (transmitter, f_0) and a high pass filter (HPF) operating in the backscatter frequency band (receiver, $2f_0\pm f_m$). The response characteristics for the diplexer filters as simulated in ADS Momentum are shown in Fig. 3b, depicting a passband roughly extending from 2.0 to 3.0 GHz for the LO port and 4.25 to 5.5 GHz for the RF port, with greater than 60 dB isolation between the two ports. The layouts for the LTSA and diplexer were combined in ADS, as shown in Fig. 3c. The LTSA and diplexer were milled on Rogers Duroid 5880 (0.020 inches, ½ oz./sqft. rolled copper) substrate.

The schematic of an RF synchronous demodulator is shown in Fig. 3d. The demodulator was constructed to retrieve the original neuropotential signals at baseband. The incident LO exciter is produced using a signal generator (2002B Wavetek) outputting a continuous wave (CW) signal whose frequency and power can be set to any value between 2.3 to 2.7 GHz and 0 to 16.7 dBm, respectively, and is further amplified through a broadband amplifier (ZHL-42 Mini-Circuits). This generated exciter passes through a band-pass filter (BPF) around f_0 to suppress the higher harmonics that are usually generated from an imperfect signal generator and augmented in the amplifier stage. The output of the amplifier is connected to another BPF around f_0, which is then connected to the LO port of the LTSA. Concurrently, the exciter is also fed to a frequency doubler (FDR-4-8 RF Bay) to generate a $2f_0$ reference used to downconvert the RF backscattered signals ($2f_0 \pm f_m$) to baseband (f_m). This downconversion is performed through a mixer (ZX05-153LH+ Mini-Circuits) where its LO port inputs the reference of $2f_0$ and its RF port inputs the backscattered signals ($2f_0 \pm f_m$) from the LTSA's RF output. Before the signals are mixed, both the reference ($2f_0$) and backscattered signals ($2f_0 \pm f_m$) pass through multiple stages of amplification through low noise amplifiers (LNA-6G RF Bay) and BPF's around $2f_0$. This preamplification and filtering is needed in order to help improve the final SNR since noise contributions nearer to the antenna cascade and will affect the final SNR more than noise introduced further down the chain. The mixer multiplies the reference LO ($2f_0$) and the backscattered RF ($2f_0 \pm f_m$) inputs to produce the baseband output (f_m). This baseband signal is then fed into an amplifier and filter (SR560, Stanford Research Systems) with a gain of 50 dB around the passband of 0.5 Hz to 3 kHz. The demodulator yielded a noise floor of around -34 dBm at baseband. The system performance is defined mostly by noise in the exciter (LO at f_0) and by the noise figures of the amplifiers in the demodulation signal chain. Noise in the microsystem originates from only a relatively few sources mainly associated with Johnson noise generated by the resistive components of the antenna and from the electrode-tissue interface. The input power of LO is limited to approximately 47 mW (16.7 dBm). Based on this excitation power, the approximate power density of the radiated fields absorbed by the head, or specific absorption rate (SAR), is less than 120 mW/kg, as computed in HFSS. This estimated SAR is in compliance with the exposure guideline set forth by U.S. Federal Communication Commission (FCC) of 1.6 W/kg for personal wireless communication devices over a volume equivalent to 1 g in the head [39].

D. Microsystem Fabrication

The neuro-recording microsystem was fabricated on a high resistivity (10 kΩ·cm) p-type (100) silicon wafer. The cross-sectional fabrication process flow is depicted in Fig. 4a. Initially, a low-stress non-stoichiometric 600 nm thick silicon nitride (SiN_x) followed by an 800 nm thick silicon dioxide (SiO_2) films were deposited using low-pressure chemical vapor deposition (LPCVD) at 250 mTorr and 800 °C and thermal wet oxidation at 1050 °C, respectively. These layers serve as isolation to avert conductive paths of subsequent layers to the silicon substrate. 1) Shallow trenches (50 μm deep) were etched into the substrate using reactive ion etching (RIE) of the SiN_x and SiO_2 films, and 30% wt. potassium hydroxide (KOH) anisotropic etching of the silicon substrate. The RIE process parameters (consistent throughout fabrication procedure) for SiN_x etching were a pressure of 50 mTorr, RF power of 150 W, CHF_3 flow rate of 50 sccm, and O_2 flow rate of 5 sccm, and for SiO_2 etching were 30 mTorr, 200 W, CHF_3 at 25 sccm, and Ar at 25 sccm. These trenches are for mounting off-chip varactors in a subsequent assembly stage. The trenches were insulated by depositing another 600 nm thick SiO_2 film on the topside using plasma-enhanced chemical vapor deposition (PECVD) at 500 mTorr and 300 °C. 2) Windows for patterning through-hole interconnects were patterned on the backside by RIE of the SiO_2 and SiN_x films. The through-hole interconnects were formed by anisotropic etching using 30% wt. KOH solution at 100°C for an etch rate of about 3.5 μm/min for 180 minutes, until the topside SiN_x was

exposed. The exposed silicon via holes on the backside were insulated by a 600 nm thick SiO_2 layer (PECVD at 500 mTorr and 300 °C). 3) A conductive film was deposited on the backside using thermal evaporation of Cr/Au (40/200 nm). The film was thickened to approximately 10 μm by electroplating (TSG-250) at a rate of 1 mA/cm^2 at 60°C. The Cr/Au film was patterned using wet etchants (1020, GE-8148) and form the two backside terminals to directly acquire neuropotentials. 4) 50 μm wide square via holes were etched into the topside SiN_x and SiO_2 films by RIE to expose the backside Cr/Au terminals. 5) Cr/Au (40/200 nm) films were thermally evaporated onto the topside to close the electrical path from backside terminals to topside contacts, completing the through-hole interconnects; allow neuropotentials acquired from backside thermals to connect to circuitry on the topside. These topside Cr/Au films also serve as bottom contacts for MIM capacitors. 6) A 200 nm thick SiO_2 layer was deposited and patterned on the topside (PECVD at 500 mTorr and 150 °C) and RIE, respectively, to form the dielectric layer of the MIM capacitors. 7) Cr/Au films (40/200 nm) were thermally evaporated onto the SiO_2 film and patterned to form the top contacts of the MIM capacitors as well as the slot antenna. Flip chip varactors were mounted into the trenches of the fabricated microsystem using silver epoxy (Epo-Tek H22) and cured at 160°C for 20 minutes. Steel wires were installed onto the backside electrical terminals for ease of subsequent testing; supplying neuropotential signals to the microsystem. The completed neuro-recording microsystem is shown in Fig. 4b.

During post-fabrication inspection, peeling of topmost Au film (antenna and top MIM electrodes) and DC leakage through MIM capacitors on several dies were observed. The metal peeling and leakage may be due to poor adhesion and non-uniformity of PECVD SiO_2, respectively. These shortcomings may be diminished by increasing the thickness of the Cr seed layer and better controlling the uniformity of PECVD SiO_2, respectively.

III. Results

The fabricated neuro-recording microsystem was tested using 1) emulated neuropotentials and 2) *in vivo* compound action potentials (CAPs) from a frog's sciatic nerve. A signal generator (Agilent 8241) was used to provide incident microwave signals in the range of 2.25 to 2.45 GHz (f_0), which was connected to the transmit port (LO) of the external interrogator. A spectrum analyzer (Agilent E4440A) was used to monitor the backscattered signals (at $2f_0 \pm f_m$). The resolution bandwidth of the analyzer was set to 1 Hz yielding a noise floor of around -135 dBm for a 1 kHz acquisition span. The analyzer was connected to the receive port (RF) of the external interrogator.

A. Emulated Neuropotentials

Emulated neuropotentials from a function generator (Agilent 33250A) were used to characterize the wireless backscattering response of the microsystem. Various waveforms (sinusoid, square, triangle), in the range of 1 to 50 mV_{pp} and 10 Hz to 5 kHz, were applied to the backside terminals of the microsystem. Incident power supplied from the signal generator ranged from 0 to 16.7 dBm (1 to 47 mW). The strength of the backscattered signals was quantified by the power of the sidebands around the second harmonic ($2f_0 \pm f_m$) collected by the external interrogator. The minimum detectable signal (MDS) was set to -130 dBm, indicating that the sidebands should be at least 5 dB greater than the noise. An example of the spectral response, a 3.4 mV_{pp} sinusoidal input at a distance of 2.5 mm, is shown in Fig. 5a. The recovered waveforms at baseband are shown in Fig. 5c, for sinusoidal, square, and triangle emulated neuropotentials of 3 mV_{pp} at 800 Hz. For a sinusoidal 1 mV_{pp} input of 1 kHz, the demodulator yielded an SNR of around 1.5. The maximum wireless detection range was limited to 15 mm for neuropotentials below 50 mV_{pp}. For neuropotentials in the range of few *millivolts*, the microsystem needed to be placed within 2 mm from the external interrogator. Measured emulated signals of 50 mV_{pp} as a function of

distance between the neuro-recording microsystem and the external interrogator are plotted in Fig. 5b. The expected wireless attenuation of these signals in the far-field is also plotted as a solid gray line in Fig. 5b for comparison. A summary of the measured specifications for the microsystem is tabulated in Table 1.

B. In Vivo Neuropotentials

The microsystem was tested using neuropotentials from the frog sciatic nerve in order to demonstrate the feasibility of embedding the microsystem in living organisms in the future. The frog was terminated immediately before conducting the experiment to ensure the viability of its nervous system. The sciatic nerve is capable of producing neuropotentials on the order of *millivolts* [40]. The magnitude of an electrical stimulation pulse determines the number of neurons recruited to generate an action potential. The superimposing of simultaneous action potentials propagating a bundle of nerves result in compound action potentials (CAPs). However, naturally evoked CAPs may measure lower in magnitude in these types of extracellular recordings because the individual action potentials are not as synchronized between the axons as in a controlled stimulation. The current stimulus was a biphasic square waveform with a pulse-width of 0.2 ms (cathodic stimulation pulse followed by anodic-charge balancing pulse). Electrodes were connected from the frog's sciatic nerve to the microsystem, which was placed within 5 mm to the external interrogator. Stimulating electrodes were connected to the sciatic nerve approximately 10 mm above the terminals of the microsystem. The CAPs were evoked at a rate of 2 to 140 Hz and were within the range of 500 to 1000 μV_{pp} as recorded by the microsystem. CAPs with amplitudes lower than 500 μV_{pp} were also evoked, but were not able to be detected by the external interrogator. These neuropotential signals are near the overall system noise level and are very difficult to directly record. However, the potential to use such an approach with improvements in demodulation technique was investigated using 128 epoch signal averaging of the repetitive CAP response to achieve an SNR improvement of 11.3. An example of the signals acquired from the frog's sciatic nerve is shown in the bottom plot of Fig. 5d, where the CAPs measured to have a V_m of 500 μV_{pp} at f_m of 140 Hz. To verify the integrity of the wirelessly recorded signals, the CAPs were also recorded directly with electrodes attached to the sciatic nerve and amplified as shown in the top plot. The spikes between the CAP waveforms are stimulation artifacts from current induced excitation of the sciatic nerve. The data are encouraging in that it suggests that future work in reducing noise in the receiver system may remove the need for averaging.

IV. Conclusion

The fabricated microsystem has demonstrated the ability to wirelessly acquire neuropotentials in an entirely passive manner by way of microwave backscattering. The neuro-recording microsystem prototype reported in this work displayed a sensitivity closer to a few *millivolts*, still an order of magnitude lower than needed for typical cortically derived neuropotentials (approximately tens to hundreds of *microvolts*). The spectral response, on the other hand, is not limited by typical bioamplifier design characteristics and extends from near DC to apparently hundreds of *kilohertz*. Thus, its bandwidth easily accommodates the characteristic frequency range of cerebral neuropotentials (10 Hz to 3 kHz).

At this stage, the sensitivity and size of the microsystem are the main challenges in deploying the microsystem for practical use in cerebral recording. Future work will focus on increasing the sensitivity and decreasing the size of the microsystem so that it may be deployed in cortical applications. One approach to enhancing sensitivity is to decrease noise, most likely due to external source coupling. Because the simplicity of the microsystem relies on its fully-passive modality and its few components, it is likely that further noise

suppression must be addressed in the design of the external receiver system. The sensitivity of the microsystem might be improved further by optimizing the design of the mixer by utilizing varactors with stronger nonlinearities to augment the modulation by neuropotentials in the generation of third-order harmonics. Furthermore, its footprint may be reduced by fabrication of a monolithic microsystem, free of any peripheral off-chip components, through deposition of ferroelectric films possessing similar nonlinear properties to varactor components [41], [42].

Acknowledgments

The authors thank Dr. Masoud Koochakzadeh for assisting in the design of the diplexer, Jaeyoong Cho for depositing PECVD films at University of Michigan, Lurie Nanofabrication Facility, Patrick Larson for his assistance with animal testing, Dr. Rainee Simons from NASA-GRC for his valuable input, and M/A-COM for free varactor samples.

This work is partially supported by the U.S. National Science Foundation under Grant ECCS-0702227, the National Institutes of Health under Grant 5R21NS059815-02, and the NASA Graduate Student Research Program fellowship NNX09AK93H.

Biography

Helen N. Schwerdt received the B.S. degree in biomedical engineering and the M.S.E. degree in electrical and computer engineering from Johns Hopkins University, Baltimore, MD, in 2008 and 2009, respectively. She is currently working towards the Ph.D. degree in electrical engineering at Arizona State University, Tempe, AZ.

Her research interests lie in microelectromechanical systems (MEMS), nonlinear microwave circuits, miniature antennas, and wireless instrumentation for biomedical and neurological applications.

Wencheng Xu received the B.S. degree in electrical engineering from Tsinghua University, Beijing, China, in 2003, and the M.S. degree in applied physics from the Hong Kong Polytechnic University, Hong Kong, China, in 2006. He is currently working towards the Ph.D. degree in electrical engineering at the School of Electrical, Computer, and Energy Engineering, Arizona State University, Tempe, AZ.

His research interests include ultrasonic resonators and piezoelectric micro- and nanosystems (microelectromechanical / nanoelectromechanical systems) for radio-frequency and biological applications.

Sameer Shekhar received the B.E. degree in telecommunication engineering from R.V. College of Engineering, Bangalore, India, in 2006 and the M.S. degree in electrical engineering from Arizona State University, Tempe, AZ, in 2010.

He is currently working with Intel Corporation as an analog engineer in Hillsboro, OR. His past work has focused on leaky-wave antennas and building electromagnetic structures. His research interest also includes analog and microwave circuits.

Abbas Abbaspour-Tamijani (S'00–M'04–SM'09) received the B.S. and M.S. degrees from the University of Tehran, Tehran, Iran, in 1994 and 1997, respectively, and the Ph.D. degree from the University of Michigan, Ann Arbor, MI, in 2003, all in electrical engineering.

He worked in industry as an Antenna and RF Engineer from 1996 to 1999. In 2004, he was a Research Fellow with the Radiation Laboratory, University of Michigan at Ann Arbor, and an RF Engineer at Motia Inc., Pasadena, CA. Later that year, he joined Arizona State University, Tempe, AZ, as an assistant professor of electrical engineering, where he conducted research on beam-steerable and reconfigurable antennas, wideband tunable filters, RF MEMS, and applications of microwave telemetry for wireless neural interfacing. During this time, his research was funded by NSF, NIH, DARPA, NASA, and industry and he was the recipient of a DARPA Young Faculty Award in 2008. In 2010, he founded Freeform Wave Technology, LLC, which is a privately held research firm focused on developing innovative RF and millimeter-wave technology solutions for various communication and sensing applications. He lives and works in Los Angeles, CA.

Dr. Abbaspour-Tamijani is a senior member of the IEEE and a member of the Microwave Theory and Techniques Society, Antennas and Propagation Society, and Engineering in Biology and Medicine Society

Bruce C. Towe received the Ph.D. degree in biomedical engineering from Pennsylvania State University, University Park, PA, in 1978.

Dr. Towe is currently on the faculty of Arizona State University, Tempe, AZ. He is active in teaching and research in the Harrington Biomedical Engineering, School of Biological and Health Sciences. His areas of specialization include bioelectronic instrumentation, biosensors, biological and medical instrumentation, and medical ultrasound.

Félix A. Miranda (M'91–SM'98) received the B.S. degree from the University of Puerto Rico, PR, in 1983, the M.S. degree from Rensselaer Polytechnic Institute, Troy, NY, in 1986, and the Ph.D. degree from Case Western Reserve University, Cleveland, OH, in 1991, all in physics.

He is currently the Chief of the Antenna and Optical Systems Branch in the Communications, Instrumentation and Controls Division at the NASA Glenn Research Center in Cleveland, Ohio. His areas of expertise are antenna technology, ferroelectric tunable microwave components, and microwave integrated circuits and devices for space and ground-based communications.

Dr. Miranda is a senior member of the IEEE, a member of the American Institute of Aeronautics and Astronautics (AIAA), a member of the American Physical Society (APS), and a member of the Forum of Industrial and Applied Physicists (FIAP). He is a member of the editorial board of Integrated Ferroelectrics (Taylor & Francis) and of the reviewer's board of the IEEE Transactions on Microwave Theory and Techniques.

Dr. Miranda has authored or co-authored more than 155 technical publications in his areas of expertise. He has written several book chapters and is the co-inventor of six U.S. patents. He is a former NASA Administrator's Fellow and received the 2001 Outstanding Technical Achievement Award from the Hispanic Engineer National Achievement Awards Conference (HENAAC). He is the recipient of the 2007 NASA Exceptional Service Medal for outstanding technical and managerial leadership in antenna and microwave technologies for space communications. He received the 2007 R&D100 award for the development of an Antenna Near-Field Probe Station Scanner and the 2010 R&D100 for the development of a Thin Film Ferroelectric High Resolution Scanning Reflectarray Antenna for Aerospace Communications. He received the 2009 Wall Street Journal's Technology Innovation Award as a runner-up in the wireless category for an invention involving MEMS based implantable systems using radio frequency telemetry. He was awarded the 2010 NorTech Innovation Award for "Radio Frequency Telemetry System for Implantable Bio-MEMS Sensors." He is

the recipient of the 2009 NASA Equal Employment Opportunity Medal and received the 2010 NASA Glenn Research Center Diversity Leadership Award for his efforts to promote and further diversity in science and technology.

Junseok Chae received the B.S. degree in metallurgical engineering from Korea University, Seoul, Korea, in 1998, and the M.S. and Ph.D. degrees in electrical engineering and computer science from University of Michigan, Ann Arbor, MI, in 2000 and 2003, respectively.

He joined Arizona State University in 2005 as an assistant professor and now he is an associate professor of electrical engineering. He has published over 85 journal and conference articles, two book chapters, one book, and holds two U.S. patents. His areas of interest are MEMS sensors/actuators, integrating MEMS with readout/control electronics, and micro-packaging. He received the 1st place prize and the best paper award in DAC (Design Automation Conference) student design contest in 2001. He is a recipient of the NSF CAREER award for his work on MEMS protein sensor array.

References

1. Hatsopoulos NG, Donoghue JP. The science of neural interface systems. Annual Review of Neuroscience. Jul.2009 32:249–266.
2. Wisneski KJ, Anderson N, Schalk G, Smyth M, Moran D, Leuthardt EC. Advanced neurotechnologies for chronic neural interfaces: new horizons and clinical opportunities. Stroke. Nov.; 2008 39(12):3351–3359. [PubMed: 18927456]
3. Leuthardt EC, Schalk G, Wolpaw JR, Ojemann JG, Moran DW. A brain-computer interface using electrocorticographic signals in humans. Journal of Neural Engineering. Jun; 2004 1(2):63–71. [PubMed: 15876624]

4. Hochberg LR, Serruya MD, Friehs GM, Mukand JA, Saleh M, Caplan AH, Branner A, Chen D, Penn RD, Donoghue JP. Neuronal ensemble control of prosthetic devices by a human with tetraplegia. Nature. Jul; 2006 442(7099):164–171. [PubMed: 16838014]
5. Wise KD, Sodagar AM, Yao Y, Gulari MN, Perlin GE, Najafi K. Microelectrodes, microelectronics, and implantable neural microsystems. IEEE Proceedings. Jul; 2008 96(7):1184–1202.
6. Harrison RR. Design of integrated circuits to observe brain activity. IEEE Proceedings. Jul; 2008 96(7):1203–1216.
7. Sodagar AM, Wise KD, Najafi K. A fully integrated mixed-signal neural processor for implantable multichannel cortical recording. IEEE Transactions on Biomedical Engineering. Jun; 2007 54(6): 1075–1088. [PubMed: 17554826]
8. Song YK, Borton DA, Park S, Patterson WR, Bull CW, Laiwalla F, Mislow J, Simeral JD, Donoghue JP, Nurmikko AV. Active microelectronic neurosensor arrays for implantable brain communication interfaces. IEEE Transactions in Neural Systems and Rehabilition Engineering. Jun.; 2009 17(4):339–345.
9. Harrison RR, Watkins PT, Kier RJ, Lovejoy RO, Black DJ, Greger B, Solzbacher F. A low-power integrated circuit for a wireless 100-electrode neural recording systems. IEEE Journal of Solid-State Circuits. Jan..2007 42:123–133.
10. Ho M, Chen H, Tseng F, Yeh S, Lu MS. CMOS micromachined probes by die-level fabrication for extracellular neural recording. Journal of Micromechanics and Microengineering. Jan..2007 17:283–290.
11. Kim S, Bhandari R, Klein M, Negi S, Rieth L, Tathireddy P, Toepper M, Oppermann H, Solzbacher F. Integrated wireless neural interface based on the Utah electrode array. Biomedical Microdevices. Dec..2009 11:453–466. [PubMed: 19067174]
12. Perlin, GE.; Wise, KD. Ultra-compact integration for fully-implantable neural microsystems. IEEE 22nd International Conference on Micro Electro Mechanical Systems; Sorrento, Italy. Jan. 2009; p. 228-231.
13. Chestek CA, Gilja V, Nuyujukian P, Kier RJ, Solzbacher F, Ryu SI, Harrison RR, Shenoy KV. HermesC: low-power wireless neural recording system for freely moving primates. IEEE Transactions on Neural Systems and Rehabilitation Engineering. Aug.; 2009 17(4):330–338. [PubMed: 19497829]
14. Rizk M, Bossetti CA, Jochum TA, Callender SH, Nicolelis MA, Turner DA, Wolf PD. A fully-implantable 96-channel neural data acquisition system. Journal of Neural Engineering. Mar..2009 6:1–14.
15. Harrison RR, Kier RJ, Chestek CA, Gilja V, Nuyujukian P, Ryu S, Greger B, Solzbacher F, Shenoy KV. Wireless neural recording with single low-power integrated circuit. IEEE Transactions on Neural Systems and Rehabilitation Engineering. Aug.; 2009 17(4):322–328. [PubMed: 19497825]
16. Sodagar, AM.; Perlin, GE.; Yao, Y.; Wise, KD.; Najafi, K. An implantable microsystem for wireless multi-channel cortical recording. IEEE International Solid-State Sensors, Actuators and Microsystems Conference; Lyon, France. Jun. 2007; p. 69-72.
17. Holleman, J.; Yeager, DJ.; Prasad, R.; Smith, JR.; Otis, B. NeuralWISP: a wirelessly powered neural interface with 1-m range. IEEE Biomedical Circuits and Systems Conference; Baltimore, MD. Nov. 2008; p. 37-40.
18. Chen H, Wu J, Hyland B, Lu X, Chen JJ. A low noise remotely controllable wireless telemetry system for single-unit recording in rats navigating in a vertical maze. Medical and Biological Engineering and Computing. May.2008 46:833–839. [PubMed: 18509686]
19. Penttilä K, Keskilammi M, Sydänheimo L, Kivikoski M. Radar cross-section analysis for passive RFID systems. IEEE Proceedings on Microwave Antennas and Propagation. Feb.; 2006 153(1): 103–109.
20. Nikitin PV, Rao KVS. Theory and measurement of backscattering from RFID tags. IEEE Antennas and Propagation Magazine. Dec.; 2006 48(6):212–218.
21. Fonseca, MA.; Allen, MG.; Kroh, J.; White, J. Flexible wireless passive pressure sensors for biomedical applications. Solid-State Sensors, Actuators, and Microsystems Workshop; Hilton Head, SC. Jun. 2006; p. 37-42.

22. Towe, BC. Passive backscatter biotelemetry for neural interfacing. IEEE/EMBS 3rd International Conference in Neural Engineering; May 2007; p. 144-147.

23. Abbaspour-Tamijani, A.; Farooqui, M.; Towe, BC.; Chae, J. A miniature fully-passive microwave back-scattering device for short-range telemetry of neural potentials. 30th Annual International Conference of the IEEE/EMBS; Aug. 2008; p. 129-132.

24. Riistama J, Aittokallio E, Verho J, Lekkala J. Totally passive wireless biopotential measurement sensor by utilizing inductively coupled resonance circuits. Sensors and Actuators A: Physical. Dec..2009 157:313–321.

25. Honig, W. Wireless passive biological telemetry system. Nov.. p. 1965U.S. Patent 3218638

26. Wansch R. Small antennas for wireless micro-systems. Active and Passive Electronic Components. Dec..2001 25:71–82. 2002.

27. Ito K, Furuya K, Okano Y, Hamada L. Development and characteristics of a biological tissue-equivalent phantom for microwaves. Electronics and Communications in Japan. 84(4):1126–1135, 2001.

28. Gabriel, C.; Gabriel, S. Report for Armstrong Laboratory (AFMC), Occupational and Environmental Health Directorate, Radiofrequency Radiation Division: AL/OE-TR-1996-0037. TX, USA: 1996. Compilation of the dielectric properties of body tissues at RF and microwave frequencies.

29. Cole KS, Cole RH. Dispersion and absorption in dielectrics. Journal of Chemical Physics. Apr.. 1941 9:341–52.

30. Balanis, CA. Advanced Engineering Electromagnetics. John Wiley & Sons; Hoboken, NJ: 1989.

31. Galejs, J. Antennas in Inhomogeneous Media. Pergamon Press; London, Great Britain: 1969.

32. Maas, SA. Nonlinear Microwave and RF Circuits. Artech House; Norwood, MA: 2003.

33. Hedderly DL. An analysis of a circuit for the generation of high-order harmonics using an ideal nonlinear capacitor. IRE Transactions on Electron Devices. Jun..1962 :484–491.

34. Balanis, CA. Antenna Theory: Analysis and Design. John Wiley & Sons; Hoboken, NJ: 2005.

35. Wheeler HA. Fundamental limitations of small antennas. IEEE Proceedings of the Institute of Radio Engineers. Mar..1947 :1479–1484.

36. Harrington RF. Effect of antenna size on gain, bandwidth, and efficiency. Journal of Research of the National Bureau of Standards—D , Radio Propagation. Jan.; 1960 64D(1):1–12.

37. Janaswamy R, Schaubert DH, Pozar DM. Analysis of the transverse electromagnetic mode linearly tapered slot antenna. Radio Science. Sept.; 1986 21(5):797–804.

38. Yngvesson KS, Schaubert DH, Korzeniowski TL, Kollberg EL, Thungren T, Johansson JF. Endfire tapered slot antennas on dielectric substrates. IEEE Transactions on Antennas and Propagation. 33(12):1392–1400, 1985.

39. Means DL, Chan KW. Evaluating compliance with FCC guidelines for human exposure to radiofrequency electromagnetic fields. Federal Communications Commission Office of Engineering and Technology OET. Jun..2001 :1–53. Bulletin 65, Supplement C.

40. Katsuki R, Fujita T, Liu T, Nakatsuka T, Nakashima M, Kumamoto E. Tramadol, but not its major metabolite (mono-o-demethyl tramadol) depresses compound action potentials in frog sciatic nerves. British Journal of Pharmacology. Aug..2006 149:319–327. [PubMed: 16921387]

41. Booth JC, Ono RH, Takeuchi I, Chang K. Microwave frequency tuning and harmonic generation in ferroelectric thin film transmission lines. Applied Physics Letters. Jul.; 2002 81(4):718–720.

42. Vorobiev A, Rundqvist P, Khamchane K, Gevorgian S. Silicon substrate integrated high Q-factor parallel-plate ferroelectric varactors for microwave/millimeter wave applications. Applied Physics Letters. Oct.; 2003 83(15):3144–3146.

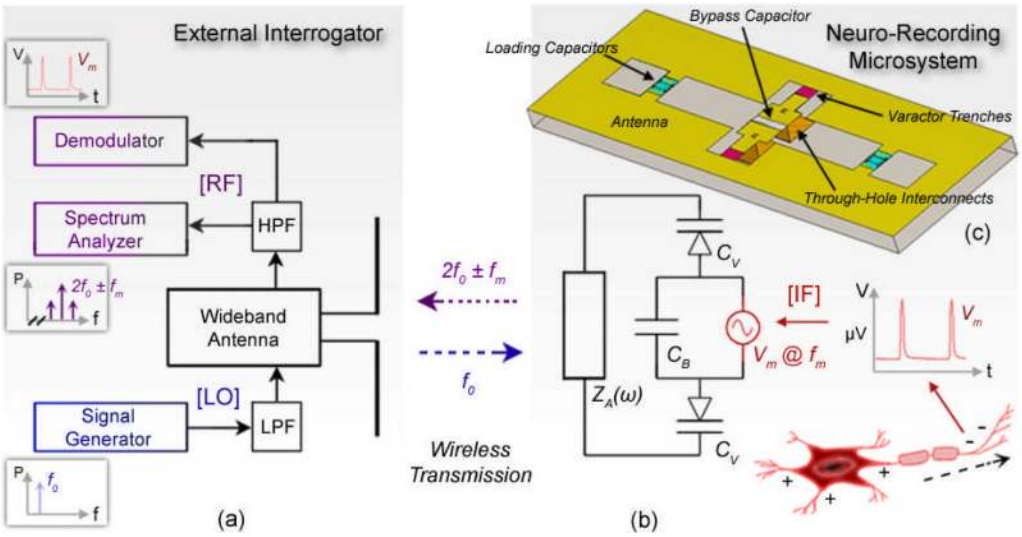

Fig. 1.

Overview of wireless fully-passive neuro-recording system. (a) Block diagram of external interrogator. The signal generator (bottom left) produces the exciter at f_0 that is fed into an LPF at the LO port of the external interrogator. This exciter is wirelessly transmitted to the microsystem, which then backscatters third-order harmonics at $2f_0 \pm f_m$. The third-order harmonics are picked up by the external interrogator and fed into an HPF at the RF output. The RF signals ($2f_0 \pm f_m$) can be detected using a spectrum analyzer, where the $\pm f_m$ sidebands are visualized in a spectral plot, and through downconversion and demodulation, where the RF signals are converted to baseband (f_m) and V_m temporal waveforms are reconstructed. (b) Basic schematic of neuro-recording microsystem circuit with illustration of cerebral source of neuropotentials (neuron). Dashed black arrow indicates direction of propagating action potentials in the axon. The spikes are conveyed as an ac signal (IF) with an amplitude of V_m and frequency of f_m that are directly supplied to the neuro-recording circuit. (c) Layout of the neuro-recording microsystem. The on-chip planar slot antenna is loaded by the capacitors located at both ends of the slot. The bypass capacitor and varactors on the topside interface directly with the neuropotentials on the backside via through-hole interconnects.

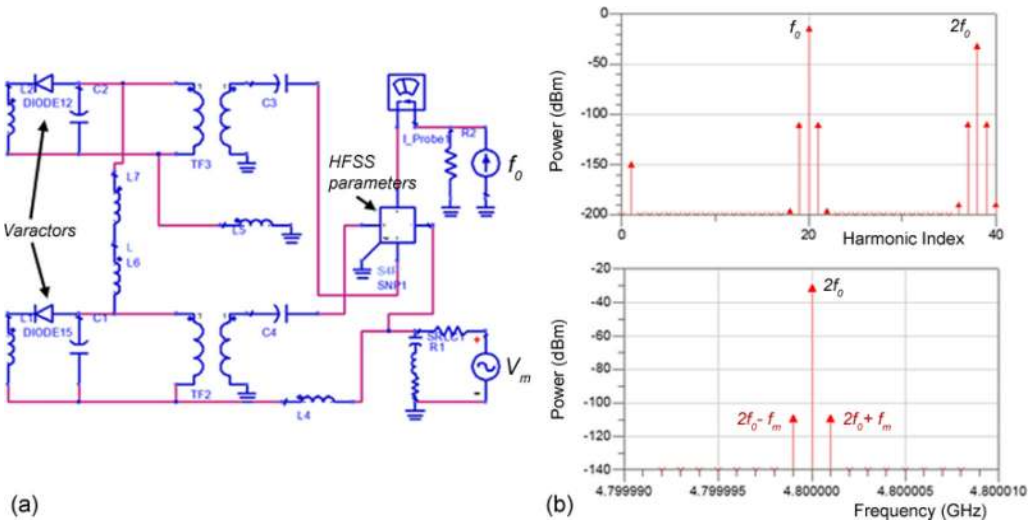

Fig. 2.

Fully-passive wireless neuro-recorder design and simulation. (a) ADS harmonic balance model of the microsystem. Varactors are seen as nonlinear diode elements with parasitic elements. The 4-port s-parameter element imports values from HFSS to model the high-frequency characteristics of the microsystem. The LO (f_0) is modeled on the top right and the neuropotentials (V_m) as an AC-source (bottom right). (b) Simulated backscattering spectral response with V_m of 100 μV_{pp} sinusoidal at f_m (IF) of 1 kHz, incident radiated power, P_0, of 1 mW (0 dBm) at f_0 of 2.4 GHz. The top plot encompasses both the incident signals (LO at f_0) as well as the backscattered third-order harmonics (RF at $2f_0 \pm f_m$).The bottom plot shows a close-up of the targeted harmonics.

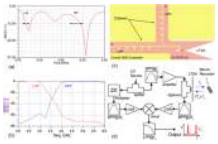

Fig. 3.

Design of the external interrogator. (a) Return loss of the linearly tapered slot antenna (LTSA). The bands of operation, LO and RF, are designated by arrows, and indicate a return loss of greater than 7 dB for these bands. (b) Frequency response of LPF used for LO (f_0) and of HPF used for RF ($2f_0$) ports of the diplexer. (c) Layout of the external interrogator with the diplexer and its filters (LPF and HPF), and the antenna (LTSA) labeled. (d) Schematic of the demodulator used to recover the original neuropotential data (f_m).

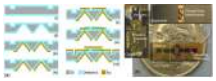

Fig. 4.

Fabrication of the neuro-recording microsystem. (a) Cross-sectional process flow: (i) Patterning and insulation of topside trenches, (ii) Bulk etching and insulation of backside through-hole interconnects, (iii) Deposition of backside conducting terminals, (iv) Topside etching of vias to expose backside metal, (v) Deposition of bottom MIM capacitor contacts and top-to-bottom conductive interconnect to bottom terminals, (vi) Deposition of silicon dioxide dielectric for MIM, and (vii) Deposition of top MIM contacts, varactor contacts in trenches, and antenna. (b) Photograph of a fabricated microsystem. A US dime lays beneath the microsystem for visual scaling. A close-up of the bypass MIM capacitor and varactor component mounted in the trench is shown on the left. The microsystem is flipped in the top figure to display the backside through-hole interconnects where neuropotentials are recorded.

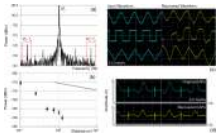

Fig. 5.

Measurement results of the fully-passive wireless neuro-recording microsystem. (a) Measured wireless spectral response of a fabricated neuro-recording microsystem at a distance of 2.5 mm, V_m of 3.4 mV_{pp} at f_m of 400 Hz, P_0 of 14.8 dBm (33.1 mW) at f_0 of 2.2 GHz. The targeted sidebands associated with the neuropotentials ($2f_0 \pm f_m$) are highlighted in red. (b) Backscattered power of targeted harmonics ($2f_0 \pm f_m$) received by the external interrogator as a function of its distance from the microsystem: in the far-field the free-space attenuation is proportional to $(4\pi R^2/\lambda)^2$, as seen by the solid gray line. An input V_m of 50 mV_{pp} at f_m of 400 Hz was used to acquire the signals. The discrepancy between the predicted power (solid gray line) and the measured power is likely due to the near-to-far-field transition. (c) Demodulated emulated waveforms of sinusoid (top), square (middle), and triangle (bottom) functions. The input emulated waveforms into the neuro-recording microsystem have a V_m of 3 mV_{pp} at f_m of 800 Hz and are shown on the left (cyan) and the wirelessly demodulated waveforms from the external interrogator are shown on the right (yellow). A low frequency noise (120 Hz) exists, and may be perceived by the slower oscillating component. (d) Measured and demodulated frog neuropotentials from the sciatic nerve. The original frog CAP waveforms as measured directly from reference wired-electrodes are shown on the top (cyan). The waveforms were measured to have a V_m of 500 μV_{pp} at f_m of 140 Hz. The wirelessly recovered neuropotentials as measured from the neuro-recording microsystem are shown on the bottom (yellow). The abrupt spikes between CAP waveforms are stimulation artifacts from current induced excitation of the nerves. The bottom recovered CAP waveforms used 128 epoch signal averaging of repetitive signals.

TABLE I

Measured specifications of the neuro-recording microsystem

Footprint	**Dimensions**	***12 × 4 × 0.5 mm^3***
Detected Input Signals	Bandwidth	*5 – 3000 Hz*
	Amplitude	*≥ 500 μV_{pp}*
	Distance	*≤ 1.5 cm*
RF Transmission	Radiated Power	*0 – 16.7 dBm*
	Frequency	*2.2 – 2.45 GHz*
RF Reception	Sideband Level	*≤-105 dBm*
	Noise Floor	*≈ -134 dBm*
	Frequency	*4.4 – 4.9 GHz*